



**HAL**  
open science

# Identifying Flow Networks in a Karstified Aquifer by Application of the Cellular Automata-Based Deterministic Inversion Method (Lez Aquifer, France)

P Fischer, Abderrahim Jardani, X Wang, H Jourde, N. Lecoq

► **To cite this version:**

P Fischer, Abderrahim Jardani, X Wang, H Jourde, N. Lecoq. Identifying Flow Networks in a Karstified Aquifer by Application of the Cellular Automata-Based Deterministic Inversion Method (Lez Aquifer, France). *Water Resources Research*, 2017, 53 (12), pp.10508–10522. 10.1002/2017wr020921 . hal-01742263

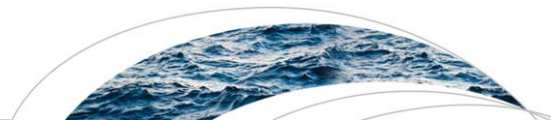
**HAL Id: hal-01742263**

**<https://normandie-univ.hal.science/hal-01742263v1>**

Submitted on 25 May 2021

**HAL** is a multi-disciplinary open access archive for the deposit and dissemination of scientific research documents, whether they are published or not. The documents may come from teaching and research institutions in France or abroad, or from public or private research centers.

L'archive ouverte pluridisciplinaire **HAL**, est destinée au dépôt et à la diffusion de documents scientifiques de niveau recherche, publiés ou non, émanant des établissements d'enseignement et de recherche français ou étrangers, des laboratoires publics ou privés.



## RESEARCH ARTICLE

10.1002/2017WR020921

### Key Points:

- We apply a newly developed inversion method to characterize a karstified aquifer
- The approach permits to map the spatial distribution of the hydraulic conductivities in the fractured and matrixial areas
- Our result model can simulate realistic flow behaviors in highly fractured aquifers

### Correspondence to:

P. Fischer,  
pierre.fischer1@univ-rouen.fr

### Citation:

Fischer, P., Jardani, A., Wang, X., Jourde, H., & Lecoq, N. (2017). Identifying flow networks in a karstified aquifer by application of the Cellular Automata-based Deterministic Inversion Method (Lez aquifer, France). *Water Resources Research*, 53, 10,508–10,522. <https://doi.org/10.1002/2017WR020921>

Received 10 APR 2017

Accepted 27 NOV 2017

Accepted article online 30 NOV 2017

Published online 15 DEC 2017

# Identifying Flow Networks in a Karstified Aquifer by Application of the Cellular Automata-Based Deterministic Inversion Method (Lez Aquifer, France)

P. Fischer<sup>1</sup> , A. Jardani<sup>1</sup>, X. Wang<sup>2</sup>, H. Jourde<sup>2</sup>, and N. Lecoq<sup>1</sup>

<sup>1</sup>Normandie Univ, UNIROUEN, UNICAEN, CNRS, Rouen, France, <sup>2</sup>Laboratoire Hydrosociétés, Université de Montpellier, CNRS, Montpellier, France

**Abstract** The distributed modeling of flow paths within karstic and fractured fields remains a complex task because of the high dependence of the hydraulic responses to the relative locations between observational boreholes and interconnected fractures and karstic conduits that control the main flow of the hydrosystem. The inverse problem in a distributed model is one alternative approach to interpret the hydraulic test data by mapping the karstic networks and fractured areas. In this work, we developed a Bayesian inversion approach, the Cellular Automata-based Deterministic Inversion (CADI) algorithm to infer the spatial distribution of hydraulic properties in a structurally constrained model. This method distributes hydraulic properties along linear structures (i.e., flow conduits) and iteratively modifies the structural geometry of this conduit network to progressively match the observed hydraulic data to the modeled ones. As a result, this method produces a conductivity model that is composed of a discrete conduit network embedded in the background matrix, capable of producing the same flow behavior as the investigated hydrologic system. The method is applied to invert a set of multiborehole hydraulic tests collected from a hydraulic tomography experiment conducted at the Terrieu field site in the Lez aquifer, Southern France. The emergent model shows a high consistency to field observation of hydraulic connections between boreholes. Furthermore, it provides a geologically realistic pattern of flow conduits. This method is therefore of considerable value toward an enhanced distributed modeling of the fractured and karstified aquifers.

## 1. Introduction

The numerical modeling of groundwater flows within heterogeneous aquifers and the assessment of their hydrodynamic properties (such as the hydraulic conductivity and specific storage coefficient) remain actually an important and complex research challenge (Hartmann et al., 2014a; White, 2002). The main difficulties faced in the modeling of these types of aquifers are due to the high contrast in the hydraulic properties at small spatial scale, at the limits between conduits, fractures, and matrix. These heterogeneities lead to complex and discontinuous patterns of groundwater flows that are mainly controlled by the geometric characteristics of the fracture or conduit networks (spatial locations, apertures, sizes, densities). Most often, fractured and karstified aquifers are modeled by using a lumped simulation method (Arfib & Charlier, 2016; Dreiss, 1982; Hartmann et al., 2014b; Kong-A-Siou et al., 2015; Labat et al., 1999; Ladouche et al., 2014; Long & Derickson, 1999), in which the whole hydrosystem is considered as a grey-box (or black-box) in order to study the responses of the system in an output signal by conceptualizing some physical processes. This method can be useful to describe the global responses of a system to a rainfall signal but it does not give precise information on the flow behavior within the aquifer. A distributed hydrodynamic simulation method is more adequate to describe the mechanistic processes of water flows within a heterogeneous aquifer. The distributed hydrodynamic simulations can be categorized in three main approaches (Ghasemizadeh et al., 2012; Hartmann et al., 2014a; Kovacs & Sauter, 2007): (i) the equivalent porous media (Abusaada & Sauter, 2013; Wang et al., 2016) in which the hydraulic features of the fractured areas are approached with equivalent continuous hydraulic properties, (ii) the double continuum (Kordilla et al., 2012; Zimmerman et al., 1993), in which the model is conceptualized with two porous continuum media (matrix and conduit) that have distinct hydraulic properties, and (iii) the combined discrete-continuum (Jaquet et al., 2004; Saller et al., 2013) in which the discrete fractures are defined by their geometries and their local apertures, their interactions with the porous matrix media are included by using exchanging flow terms.

The characterization of the spatial distribution of the hydraulic properties is commonly provided from an inversion process coupled to a hydraulic tomography approach (Bohling et al., 2002; Cardiff & Kitanidis, 2009; Wang et al., 2017; Yeh & Liu, 2000; Zhu & Yeh, 2005). This approach consists of a joint analysis of a set of piezometric data collected as the responses of a water extraction during multiple pumping tests. Both steady state and transient hydraulic tomography have been considered in previous works. In a transient hydraulic experiment, both hydraulic conductivity and specific storage influence hydraulic head distribution (Castagna et al., 2011; Sharmeen et al., 2012; Zhu & Yeh, 2005), thus, more unknown parameters need to be estimated compared to a steady state experiment where drawdown data depend exclusively on hydraulic conductivity (Cardiff et al., 2009; Wang et al., 2016; Yeh & Liu, 2000).

The efficiency of the characterization depends on the number and spatial disposition of the boreholes used in the investigation. However, in the practice cases, the number of wells is usually insufficient to reduce the uncertainty and uniqueness of the solution. To overcome these difficulties, a priori knowledge is used to constrain the inverse problem. The geostatistical approach is widely applied to constrain the hydraulic tomography particularly for porous aquifers with a moderate variability in hydraulic conductivity (Fischer et al., 2017a; Hoeksema & Kitanidis, 1984; Lee & Kitanidis, 2014). To deal with discrete spatial patterns, the method was advanced by replacing the Gaussian prior model by a Laplace prior (or total variation prior) in the Bayesian framework (Lee & Kitanidis, 2013).

However, in the case of highly heterogeneous and complex aquifers, the use of geostatistical constraints can lead to unrealistic models dominated by a relatively smooth variability of the hydraulic properties.

In this paper, we apply a novel structural inversion method, the Cellular Automata-based Deterministic Inversion (CADI), to invert the steady state hydraulic head data recorded during a hydraulic tomography to image the spatial distribution of the hydraulic transmissivities in the fractured and karstified Lez aquifer (Southern France). The theoretical aspects of the CADI method have been developed in a previous article (Fischer et al., 2017b). This method is based on the Cellular Automata (CA) concept to parameterize the model. It permits a deterministic inversion of linear structures which is interesting for the modeling of fractures and karstic conduits. The paper is developed as follows: in the first section, we present the CADI algorithm and the concept used to parameterize the model and the inverse problem. Then, in the second section, we present investigations on the experimental site. Finally, we discuss the results of the application of the proposed inverse method to map the hydrodynamic properties of a karstified and fractured aquifer.

## 2. Methodology

### 2.1. Model Parameterization

We dedicate this section to describe briefly the main concepts of the CADI method. For more details about the theory of this method, we invite the readers to refer to Fischer et al. (2017b).

A Cellular Automata (CA) is a mathematical concept that permits the generation of discrete time-evolving cells grids. At a given CA time step ( $t_{CA}$ ), the states of the cells is simultaneously modified following a global transition rule which involves the states of the cells in the neighborhood of each cell of the grid (Von Neumann & Burks, 1966).

The model in the CADI method is built as a lattice space  $\Gamma$  discretized in  $m$  squared property cells (in our case transmissivities) which are grouped in  $m_{CA}$  different CA pilot subspaces noted  $\phi_i, i \in [1, m_{CA}]$  (with  $m_{CA} \ll m$ ). The cells in a CA subspace can have two possible states: (i) state "matrix" with a transmissivity value  $\beta_{matrix}$  or (ii) state "conduit" with a transmissivity value  $\beta_{conduit}$ . The global structural distribution of the transmissivities in the model  $\Gamma$  is, thus, monitored by the different CA subspaces. Each subspace is piloted by a weighting distribution assigned to the neighborhood of each cell of the subspace (noted  $N$ ). This distribution is set up among an inner circle of "activator" "matrix" neighbor cells and an outer circle of "inhibitor" "matrix" neighbor cells (Figure 1). An "activator" "matrix" neighbor will tend to transform a given cell of the subspace (in grey in Figure 1) in a state "matrix," while an "inhibitor" "matrix" neighbor will tend to transform this cell in a state "conduit." These circles are also radially split in eight weighting sectors for a higher weight distribution possibility. At a CA time step  $t_{CA}$ , a global transition rule compares,

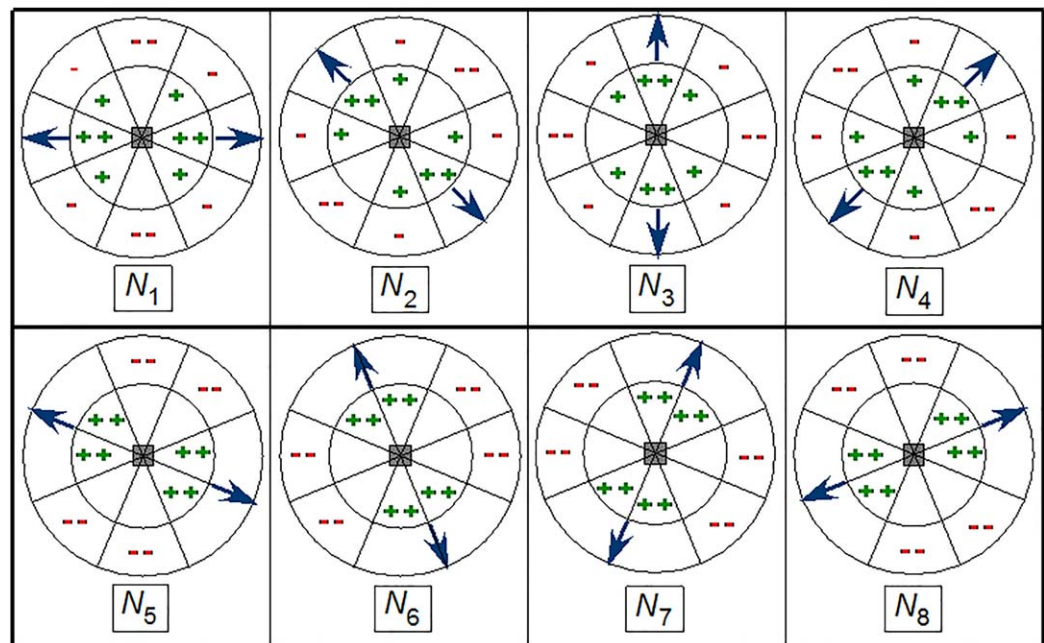


**Figure 1.** Scheme of the eight different weighting distributions  $N$  possibilities to parameterize the CA subspaces. Each distribution defines a different direction for the conduit-state generation shown by the arrows. The dual radius neighborhood is described here for a given cell in grey (the other cells are not shown for a reason of readability). In the configurations  $N_i, i \in [1, 4]$ , the circles are defined by an inner circle of radius 2 cells and an outer circle of radius 6 cells, and in the configurations  $N_i, i \in [5, 8]$ , the circles are defined by an inner circle of radius 4 cells and an outer circle of radius 5 cells. The neighbor cells of the greyed cell are split in eight internal “activator” weighting sectors and eight external “inhibitor” weighting sectors represented by the two radially split circles. A neighbor cell in state matrix can be associated (given its position in the neighborhood) to a positive weight “+ +” which is twice higher than a “+” weight, or to a negative weight “- -” which is twice higher than a “-” weight, or to a null weight in the empty sectors and beyond the neighborhood.

alternatively for each cell of the subspace, the cells in state “matrix” in the “activator” and “inhibitor” sectors of its neighborhood. For example, for a given cell, if the sum of “matrix”-state weights in its activator sector is higher than the “matrix”-state weights in its inhibitor sector, then this cell will become “matrix” in the next time step  $t_{CA} + 1$ , and in the opposite case this cell will become “conduit.” In the CADI algorithm, we configured eight different weighting distribution possibilities  $N_i, i \in [1, 8]$  which define eight different directions of propagation for the conduit in a CA subspace (see the eight configurations in Figure 1). After several successive CA time steps transitions, a subspace  $\phi$  will converge to a stable geometry noted  $\hat{\phi}$  which depends on the weighting distribution chosen for  $N$ .

The eight configurations aforementioned are considered as the different possibilities for the CA subspace parameterization during the structural optimization of the inversion process. Thus, in the CADI method a converged CA subspace  $\hat{\phi}(N, \beta)$  is parameterized by one of the eight weighted neighborhood configuration  $N_i, i \in [1, 8]$  as structural parameter and by the transmissivity values  $\beta = [\beta_{matrix}, \beta_{conduit}]$  as property parameter. The global partitioned model composed of all converged CA subspaces  $\phi_i, i \in [1, m_{CA}]$  will be referred to as  $\Gamma(\mathbf{P}_N, \mathbf{P}_\beta)$  with  $\mathbf{P}_N$  a  $m_{CA}$  vector of the different structural parameters piloting each CA subspace and  $\mathbf{P}_\beta$  a  $2m_{CA}$  vector of the  $\beta_{conduit}$  and  $\beta_{matrix}$  transmissivity values in each CA subspace of the model.

Initially in the CA temporal process, the whole model starts in an entire matrix state with only a single cell in state conduit. In the first CA time step, the conduit appears in the subspace of this initial cell, and as it arrives to the limit of this subspace it will potentially enter new subspaces (by local symmetry at the boundary between these subspaces) with another generation direction. Thus, from a unique conduit cell, the different subspaces permit the generation of a complex conduit network model at the end of the convergence of all CA (Figure 2).

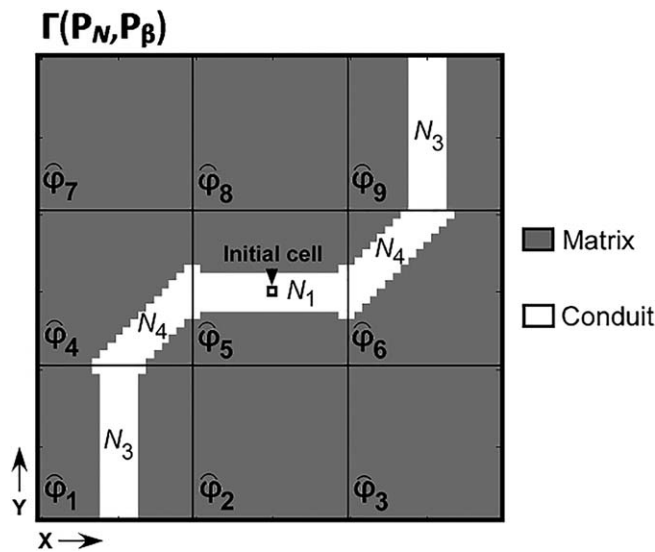


**Figure 2.** Presentation of a model in the CADI algorithm. Here the model is partitioned in nine subspaces controlled by CA. The model is parameterized by a structural parameter  $\mathbf{P}_N$  (here  $\mathbf{P}_N(5)=N_1$ ;  $\mathbf{P}_N(4)=\mathbf{P}_N(6)=N_4$ , and  $\mathbf{P}_N(1)=\mathbf{P}_N(9)=N_3$  (see Figure 1)) and a property values parameter  $\mathbf{P}_\beta$  (here every subspace is defined by the same  $\beta$  but it could vary in each subspace). Initially the whole model is considered as matrix, except an initial conduit cell. Within the CA time process, the conduit is generated from this initial cell and propagates through the model depending on the subspaces structural parameters until it reaches a global converged geometry.

### 2.2. Inverse Problem

In the Bayesian framework, the inverse problem retrieves a model matching the observed data and respecting the priori information (Tarantola & Valette, 1982). The optimization of the unknown parameters (here structural and property parameters) can be achieved by using an iterative deterministic algorithm that minimizes sequentially the following objective functions:

$$\Psi_{structure}(\mathbf{P}_N) = \frac{1}{2} (\mathbf{d}_{obs} - f(\Gamma(\mathbf{P}_N, \mathbf{P}_\beta)))^T \mathbf{C}_d^{-1} (\mathbf{d}_{obs} - f(\Gamma(\mathbf{P}_N, \mathbf{P}_\beta))) + \frac{1}{2} (\mathbf{P}_{N,prior} - \mathbf{P}_N)^T \mathbf{C}_{P_N}^{-1} (\mathbf{P}_{N,prior} - \mathbf{P}_N) \quad (1)$$

$$\Psi_{properties}(\mathbf{P}_\beta) = \frac{1}{2} (\mathbf{d}_{obs} - f(\Gamma(\mathbf{P}_N, \mathbf{P}_\beta)))^T \mathbf{C}_d^{-1} (\mathbf{d}_{obs} - f(\Gamma(\mathbf{P}_N, \mathbf{P}_\beta))) + \frac{1}{2} (\mathbf{P}_{\beta,prior} - \mathbf{P}_\beta)^T \mathbf{C}_{P_\beta}^{-1} (\mathbf{P}_{\beta,prior} - \mathbf{P}_\beta) \quad (2)$$

with  $\mathbf{d}_{obs}$  the vector of  $n \times I$  observed data (such as hydraulic responses from pumping tests),  $\mathbf{P}_{N,prior}$  and  $\mathbf{P}_{\beta,prior}$  the a priori information to constrain the inversion of the structural and property parameters,  $\mathbf{C}_d$  a  $(n \times n)$  covariance matrix of uncertainties on data, and  $\mathbf{C}_{P_N}$  a  $(m_{CA} \times m_{CA})$  and  $\mathbf{C}_{P_\beta}$  a  $(2m_{CA} \times 2m_{CA})$  covariance matrices of uncertainties on prior parameters.  $f(\Gamma(\mathbf{P}_N, \mathbf{P}_\beta))$  denotes the nonlinear forward problem operator that links the hydraulic head data and the transmissivity field.  $\Gamma(\mathbf{P}_N, \mathbf{P}_\beta)$  is the spatial partition of the transmissivity model  $\Gamma$  that is parameterized by the CA via the structural parameters  $\mathbf{P}_N$  and its property parameters  $\mathbf{P}_\beta$ .

The inversion process is conducted sequentially. First, the parameters  $\mathbf{P}_N$  and  $\mathbf{P}_\beta$  are initialized with reasonably chosen structural directions and transmissivity values for each subspace of the model. Then, the structural parameter  $\mathbf{P}_N$  is iteratively estimated with the fixed initial transmissivity model  $\mathbf{P}_\beta$ . Afterward, once the structural geometry is optimized, the spatial distribution of the transmissivity parameters  $\mathbf{P}_\beta$  is reconstructed considering this optimized structural geometry.

### 2.3. Optimization and Uncertainties Estimation

The optimization process begins with a sensitivity analysis: a local "One-factor-At-the-Time" (OAT) perturbation method, according to the classification in Pianosi et al. (2016). The structural sensitivity analysis considers the eight different neighborhood configurations (Figure 1) as structural parameters possibilities in each CA subspace  $\mathbf{P}_\beta$  in order to modify the conduit network and minimize the difference between the modeled data to the observed data. This sensitivity analysis establishes a  $(8 \times m_{CA})$  sensitivity matrix  $\mathbf{S}$ .

At a  $k$ th iteration, for a modification in a CA subspace  $j$  by testing a configuration  $N_i$ , the element  $(i, j)$  of the matrix  $\mathbf{S}$  is calculated as:

$$\mathbf{S}^k(i, j) = \left( \mathbf{d}_{obs} - f \left( \Gamma \left( \mathbf{P}_N^k \Big|_{\mathbf{P}_N^k(j)=N_i}, \mathbf{P}_\beta \right) \right) \right)^T \mathbf{C}_d^{-1} \left( \mathbf{d}_{obs} - f \left( \Gamma \left( \mathbf{P}_N^k \Big|_{\mathbf{P}_N^k(j)=N_i}, \mathbf{P}_\beta \right) \right) \right) + \frac{1}{2} (\mathbf{P}_{N,prior}(j) - N_i)^T \mathbf{C}_{P_N}^{-1} (\mathbf{P}_{N,prior}(j) - N_i) \quad (3)$$

where  $f \left( \Gamma \left( \mathbf{P}_N^k \Big|_{\mathbf{P}_N^k(j)=N_i}, \mathbf{P}_\beta \right) \right)$  represents the data modeled through the local subspace parameter perturbation and  $\mathbf{P}_{N,prior}(j) - N_i$  represents the gap between the local prior direction and the perturbation direction.

The new structural parameter  $\mathbf{P}_N^{k+1}$  is updated with the minimal value found in the matrix  $\mathbf{S}$  at the index  $(i, j)_{min}$  (where  $i$  represents the new configuration  $N_i$  for the subspace  $j$ ). The updated parameter is built as a unique local improvement:  $\mathbf{P}_N^{k+1} = \mathbf{P}_N^k$  except for  $\mathbf{P}_N^{k+1}(j_{min}) = N_{i_{min}}$ . This update will generate a new structure for the iteration  $k+1$ . The same sensitivity analysis is repeated at each iteration until there is no more possible improvements in the structure.

Then, the uncertainties of the inverted structure are estimated from the last iteration sensitivity matrix, the prior uncertainties, and the value of the objective function:

$$\mathbf{C}_{\mathbf{P}_N}^{post}(j) = \left( \frac{1}{8} \sum_{i=1}^8 \hat{\mathbf{S}}(i, j) - \Psi_{structure}^{post} + \mathbf{C}_{\mathbf{P}_N}^{-1}(j, j) \right)^{-1} \quad (4)$$

with  $\mathbf{C}_{\mathbf{P}_N}^{post}(j)$  the structural uncertainty for the subspace  $j$ ,  $\hat{\mathbf{S}}$  the last iteration sensitivity matrix and  $\Psi_{structure}^{post}$  the value of the objective function after optimization. If a subspace conduit is well-constrained its value  $\mathbf{C}_{\mathbf{P}_N}^{post}$  should be low.

After the structural optimization, a second optimization is led on the subspaces conduit and matrix transmissivity values  $\mathbf{P}_\beta$ , for the previously inverted structure. This optimization is an iterative process using a finite difference sensitivity analysis. The  $(n \times 2m_{CA})$  Jacobian sensitivity matrix is defined for its index  $(i, j)$  as:

$$\mathbf{J}(i, j) = \left. \frac{\partial f_i}{\partial \mathbf{P}_\beta} \right|_{\mathbf{P}_\beta(j) = \mathbf{P}_\beta(j) + \Delta \mathbf{P}_\beta} \quad (5)$$

with  $\Delta \mathbf{P}_\beta$  the finite difference step,  $f_i$  the forward problem variation on a data  $i$  for a variation on  $\mathbf{P}_\beta(j)$ .

At an iteration  $k$ , the updated values  $\mathbf{P}_\beta^{k+1}$  are calculated from a Newton linearization:

$$\begin{aligned} \mathbf{P}_\beta^{k+1} = & \mathbf{P}_\beta^k + \left( (\mathbf{J}^k)^T \cdot \mathbf{C}_d^{-1} \cdot \mathbf{J}^k + \mathbf{C}_{\mathbf{P}_\beta}^{-1} \right)^{-1} \cdot (\mathbf{J}^k)^T \cdot \mathbf{C}_d^{-1} \cdot \left( \mathbf{d}_{obs} - f \left( \Gamma \left( \mathbf{P}_N, \mathbf{P}_\beta^k \right) \right) \right) \\ & + \mathbf{C}_{\mathbf{P}_\beta}^{-1} \cdot \left( \mathbf{P}_{\beta, prior} - \mathbf{P}_\beta^k \right) \end{aligned} \quad (6)$$

This iterative process continues until an acceptable convergence of the objective function is achieved.

Then, the uncertainties of the property values are estimated from the last iteration Jacobian matrix  $\mathbf{J}^{post}$  with the posterior covariance matrix  $\mathbf{C}_{\mathbf{P}_\beta}^{post}$ :

$$\mathbf{C}_{\mathbf{P}_\beta}^{post} = \left( (\mathbf{J}^{post})^T \cdot \mathbf{C}_d^{-1} \cdot \mathbf{J}^{post} + \mathbf{C}_{\mathbf{P}_\beta}^{-1} \right)^{-1} \quad (7)$$

The diagonal entries of this matrix give the variances of the property values. The square root values of these entries represent the standard deviation of the uncertainties on the estimated transmissivity field.

### 3. Application

#### 3.1. Site Presentation

The Terrieu experimental site is located in the North of Montpellier, Southern France (Figure 3a). The site has been performed for the hydrodynamic studies of the Lez aquifer that is mainly composed of Early Cretaceous and Late Jurassic limestones. This site is one of the sites of the French research network SO Karst which was developed to monitor the karstic aquifers in France (Jourde et al., 2011; www.sokarst.org).

The Terrieu site sits on a local monocline structure that trends NE-SW and dips at about 15–20° toward NW. The surface area of the experimental site is about 2,400 m<sup>2</sup> (40 m × 60 m). Detailed fracture mappings, conducted at the ground surface of the site and nearby outcrops, have indicated that two major fracture sets (trending ENE-WSW and NW-SE, respectively) are present in the study area (Jazayeri Noushabadi, 2009; Wang et al., 2016).

Twenty-two boreholes have been drilled at the site to study the local-scale hydraulic behavior of the aquifer (Figure 3b). These boreholes are vertical and have a mean total drilled depth of 55 m. Downhole videos recorded in some boreholes have shown that the upper 30–40 m of the drilled formations are largely comprised of thin-layered, marly, early Cretaceous limestones while the lower part mainly consists of purer, massive, and nonaquifer late Jurassic limestones. The early Cretaceous limestone has a low permeability therefore it forms a confined upper boundary for the aquifer existing at the interface between these two units. A number of well-developed karstic conduits, with apertures up to 50 cm, have also been identified on downhole video logs. These karstic conduits were found to be present at a depth between 35 and 40 m (Jazayeri Noushabadi et al., 2011; Wang et al., 2016) at the interface of the aforementioned two units. The observed local orientation of the karstic conduits is indicated as green lines in Figure 3c. The extent of the

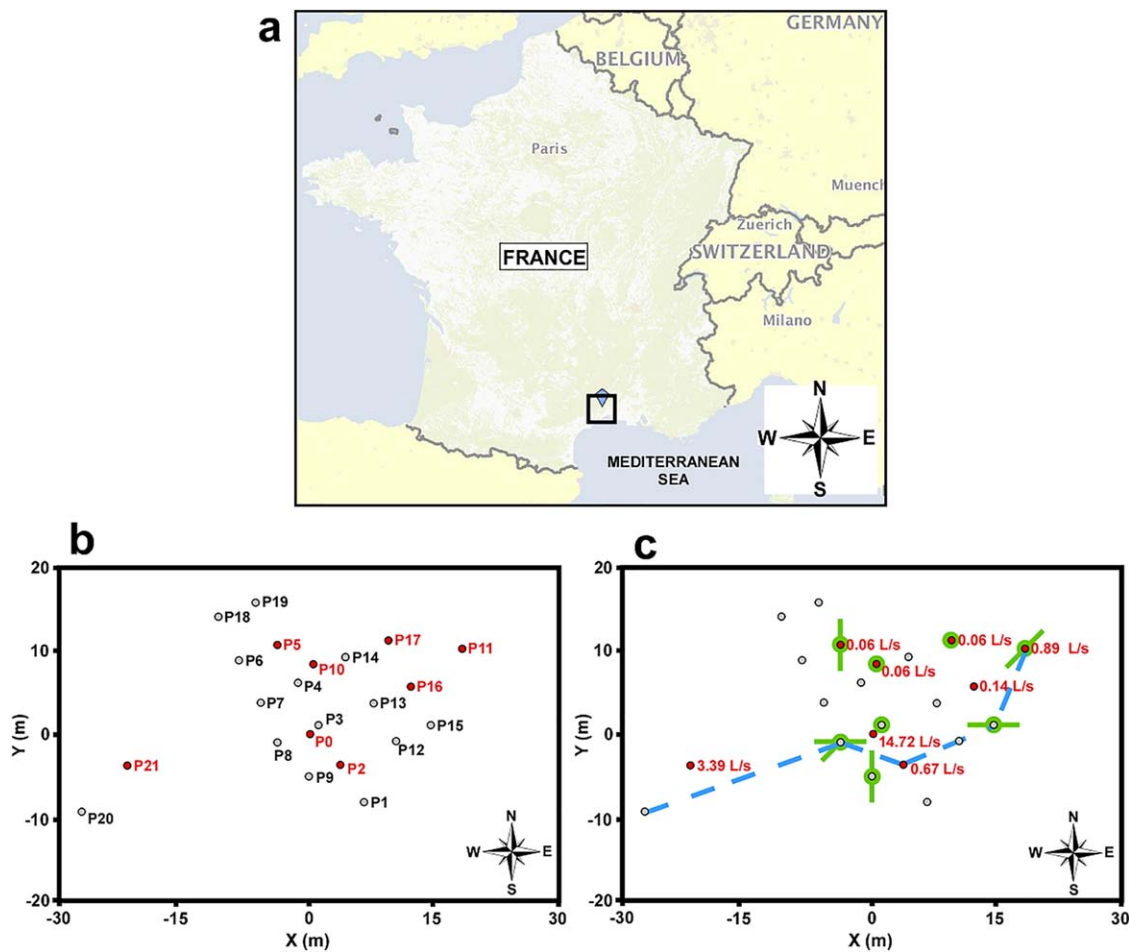


**Figure 3.** (a) Map indicating the location of the experimental site. The black square indicates the location of the Lez aquifer in which the Terrieu site is included. (b) Distribution of 22 boreholes of the Terrieu experimental site. The red dots indicate the boreholes where the pumping tests were performed while the grey dots indicate the measurement boreholes. (c) Pumping rates (red captions). Inferred principal flow path connectivity (blue dotted lines) and local karstic conduits (green lines) based on downhole videos, well logs, and packer tests. The orientation of the green lines indicates the orientation of local karstic features observed on downhole videos. A green dot indicates that no karstic features were seen in this borehole.

lower rock unit is unknown due to limited drilled depth (maximum of 60 m). Well logs (temperature and electrical conductivity) and straddle packer tests have shown that a preferential flow path (blue line in Figure 3c) exists along the major bedding plane corresponding to the interface between the two major rock units (Dausse, 2015; Jourde et al., 2002). All the observations from downhole videos, well logs, and packer tests have led to the conceptual model that a network of interconnected karstic conduits developed along an important bedding plane comprises the main flow paths of the experimental site (Wang et al., 2016).

Eight cross-hole pumping tests, in the form of hydraulic tomography, have been performed at the experimental site. The applied flow rate of each pumping test ranges from 0.2 to 53 m<sup>3</sup>/h depending on the well productivity and whether the well is connected to a high-permeability feature (Figure 3c). The drawdown of water table level generated by the pumping tests did not reach to the depth of the important bedding plane where main flow occurs; this means that the karstic network was saturated during the pumping tests. All tests reached steady state. The field-scale hydraulic tomography yielded a total number of 168 drawdown steady state measurements, which is the main data set of the present work.

This set of drawdown responses represents the observed data used in the inversion process, while the inferred preferential flow path and local conduits direction information presented in Figure 3c are not taken into account in the inversion but will be used for evaluating the effectiveness of the inversion results.

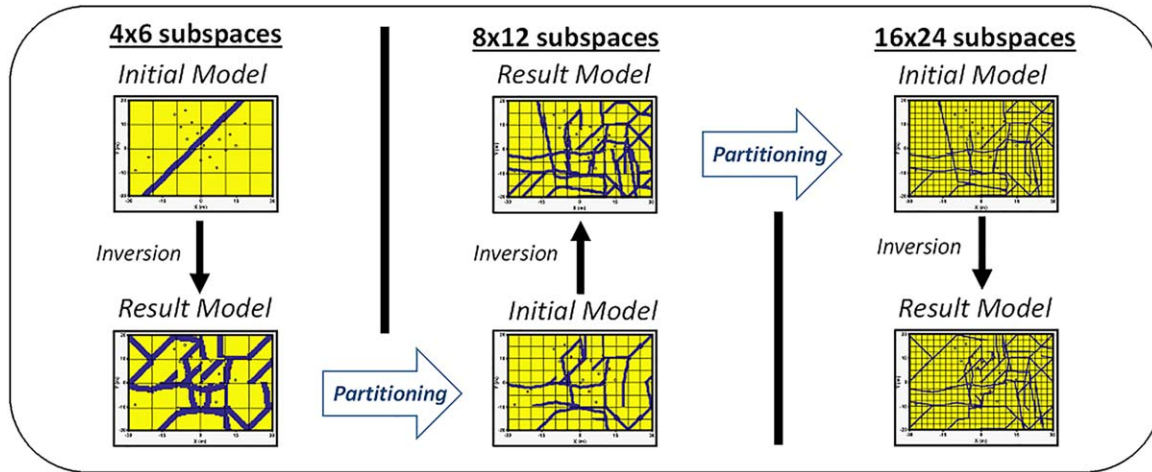


**Figure 4.** Schematic showing the sequential series of inversions led to obtain the final flow network model. The initial model was partitioned with  $4 \times 6$  subspaces for its inversion. The inverted flow network model was then used as a new initial model for an inversion with  $8 \times 12$  subspaces. The same operation was repeated on last time so that our final flow network has a partitioning of  $16 \times 24$  subspaces.

### 3.2. Modeling Method

We have applied the CADI method to image the hydraulic transmissivity distribution at the Terrieu site from the joint inversion of the set of 168 steady state drawdown data. A two-dimensional equivalent porous medium parameterization was adopted to model the domain. The porous medium was distributed in two states: bedding plane fissured matrix (CADI matrix state) or karstic conduit (CADI conduit state). We adopted an evolving meshing, that is, for each iteration, refined preferentially at the boundaries of the conduits. This avoids an over-meshing of the model, especially in the matrix zones and, thus, reduces the computation time of the forward problem solver. The forward problem (i.e., steady state diffusion equation in saturated porous media) was solved using a commercial software (COMSOL Multiphysics). The inversion process was implemented as a MATLAB code that is connected to the COMSOL solvers via a local server. The local flow network model was enclosed in a large regional buffer zone ( $1,000 \times 1,000 \text{ m}^2$ ) to reduce the influence of the boundaries conditions.

Based on a multiscale inversion method (Grimstadt et al., 2003), the flow network model was sequentially partitioned during the inversion process (see Figure 4).

The different inversion parameters chosen for the final inversion ( $16 \times 24$  CA subspaces) are presented in Table 1. The property value parameter  $\beta$  was chosen to define the exponent of the transmissivity ( $\log_{10}(T)$ ). Thus, the prior standard deviation also applies to the exponent ( $T \times 10^{\pm\sigma_T}$ ). The initial transmissivities values were chosen according to the values found during the field characterizations done by Jazayeri Noushabadi (2009) and Dausse (2015). We did not make any prior assumption on the structure directions in  $\mathbf{P}_N$  and  $\mathbf{C}_{P_N}$ .

**Table 1**  
List of the Inversion Parameter Values Chosen for the Final Inversion ( $16 \times 24$  Subspaces)

| Parameter   | Value   |
|---|---|
| Model dimension                                     | $X = [-30, 30] \text{ m}; Y = [-20, 20] \text{ m}$  |
| Partitioning/total cells amount ( $Y \times X$ )    | $16 \times 24 / 320 \times 480$   |
| Conduit aperture                                    | 50 cm   |
| Data uncertainties                                  | $\mathbf{C}_d = \sigma_{data}^2 \times \text{Id}(n); \sigma_{data}^2 = 0.01 \text{ m}$  |
| $\log_{10}$ transmissivity prior standard deviation | $\mathbf{C}_{P_\beta} = \sigma_T^2 \times \text{Id}(2m_{CA})$   |
| Initial $\log_{10}$ transmissivities                | $\sigma_T^2 = 0.001$ for the conduits; $\sigma_T^2 = 1$ for the matrix<br>$\beta_{conduit} = -1 (10^{-1} \text{ m}^2/\text{s}); \beta_{matrix} = -8 (10^{-8} \text{ m}^2/\text{s})$<br>$\beta_{regional} = -2 (10^{-2} \text{ m}^2/\text{s})$ |
| Finite difference step                              | $\Delta \mathbf{P}_\beta = 10^{-4}$   |
| Observation data ( $\mathbf{d}_{obs}$ )             | 168 steady state drawdown responses   |

We began the inversion with a model partitioned in a large discretization  $4 \times 6$  CA subspaces. In the flow network model, the karstic conduit was generated from an initial fracture cell placed at the P8 borehole (Figure 4). This choice was made based on field hydrogeological knowledge that P8 has the highest probability of intersecting the main flow path. The initial network was a simple conduit with a direction choice based on the principal flow path direction and with an aperture of 2 m. The remaining parts of the model were assigned with a transmissivity of matrix. As the structural geometry for this initial conduit was optimized, we added a second conduit in the model, orthogonally to the principal flow path and intersecting P8, and we led the structural inversion with these two principal conduits directions. When the inversion process found a  $4 \times 6$  subspaces result model, we refined the obtained solution to a model partitioned in  $8 \times 12$  subspaces (a CA subspace was divided into four new ones with the same parameters) and used it as initial model for a more precise inversion solution with conduits with an aperture of 1 m. Finally, we partitioned once more this new  $8 \times 12$  solution into a  $16 \times 24$  subspaces model which was once again used as the initial model for a final inversion solution with conduits with an aperture of 50 cm. This sequential modeling reduces the inversion time and allows interpretation of the importance of the flow paths found according to their emergence at different scales during the inversion process and thus their influence on the convergence of the objective function.

### 3.3. Results and Discussion

The simulated hydraulic heads from the final emergent flow network model show a high correlation to the field measurements (Figure 5a). It can be seen that a higher degree of difference between the simulated and measured hydraulic head exits for small drawdowns. This may due to the fact that the small hydraulic drawdowns are more sensible to microfractures that were embedded in the equivalent porous matrix in the current model. The resulting karstic flow network model from the inversion process is presented in Figure 5b. The hydraulic transmissivity of the bedding plane fissured matrix was only slightly perturbed (i.e., a small deviation from the initial value of  $10^{-8}$  m<sup>2</sup>/s) during the entire inversion process (Figure 5b), the drawdown data were essentially reproduced only by the karstic network geometry. The emergent flow network shows a high consistency with field observations shown in Figure 3c in terms of connectivity between boreholes (Figure 5c) and local direction of karstic conduits (Figure 5d). The simulated drawdown maps from the resultant flow network model are presented in Figure 6.

The simulated karstic network structure in the Terrieu experimental site investigated through the hydraulic tomography can be schematized using the emergent flow network model as shown in Figure 7. This schema conceptualizes the site in three dimensions taking into account the slope of the bedding plane.

The maps of the simulated drawdowns (Figure 6) using the final flow network model highlight the high degree of heterogeneity of the experimental site. The steady state drawdown cone of each pumping test is highly irregular, and the shape of the drawdown cone can have very different geometry in different pumping tests. Three types of behaviors can be distinguished: (i) pumping in the nonkarstified bedding plane matrix (P2, P10, P17) associated with a low pumping rate and a small influence zone of drawdown localized around the pumping borehole; (ii) pumping in low-productivity conduits (P5, P11, P16) associated with a low pumping rate and a large influence zone of small drawdowns covering the entire field; and (iii) pumping in high-productivity conduits (P0, P21) associated with a high pumping rate and a large influence zone of drawdowns impacting the whole field. In our model, pumping in the matrix only induces a response in the vicinity of the pumped well, while pumping in the conduit network induces responses impacting significantly a much larger impact area (delineated by dotted white lines in Figure 6). This shows that the global flows in the model are controlled by the karstic conduits, which can be linked to the real behavior of the site in which flows follow the important discontinuities (Jourde et al., 2002). The modeled steady state drawdowns were compared to the field observations made by Jazayeri Noushabadi (2009) and Dausse (2015), and they appear to be similar to the estimated drawdowns from the field pumping tests.

To verify the results, we have compared the inverted flow network to the mapped connectivity and local direction knowledges gained from slug tests and downhole videos (Figure 3c). This information was not taken into account during the inversion process, but they permit to assess the effectiveness of the CADI approach with the steady state drawdown responses.

The observed connectivity described in Figure 3c between P20, P8, P2, P12, P15, and P11 can be reproduced by the inverted flow network model (Figure 5c). However, the drawdown map for P2 (Figure 6)

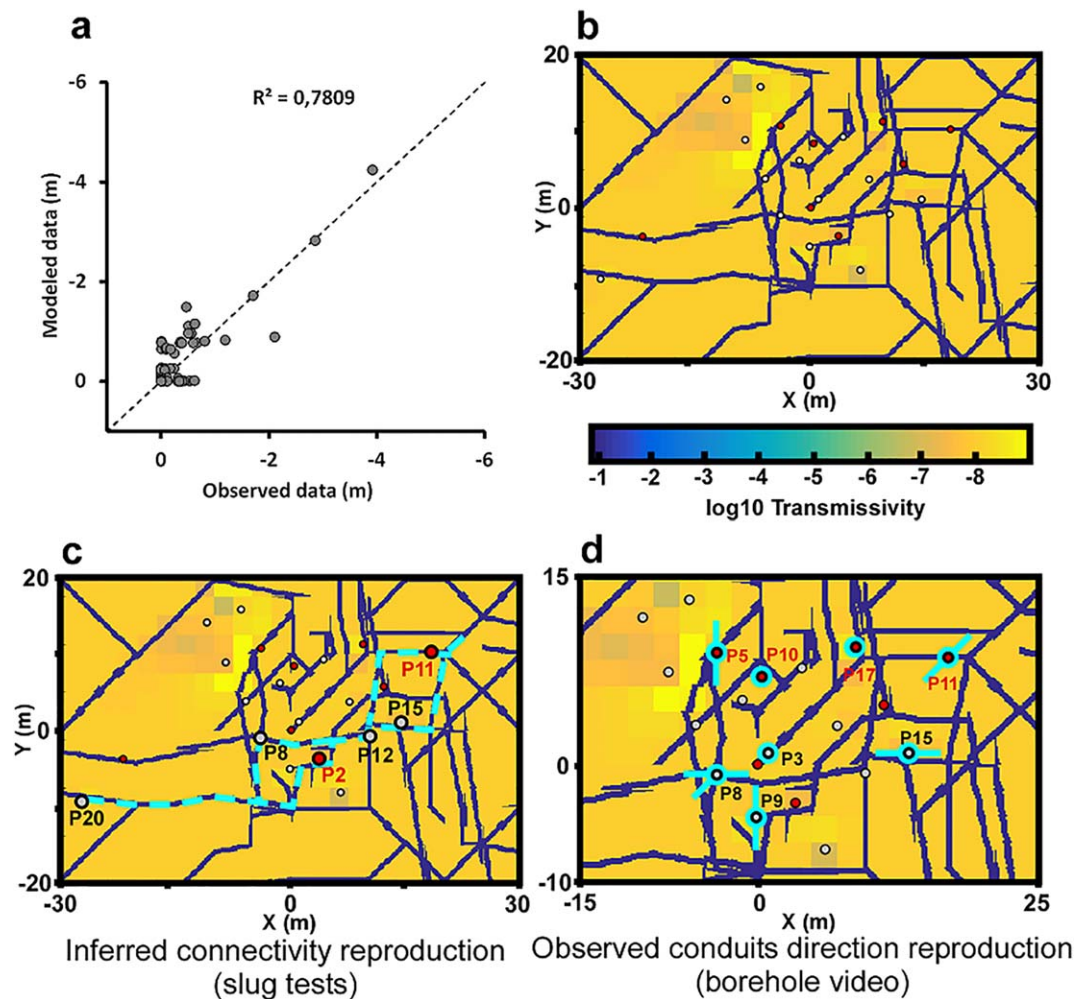


**Figure 5.** (a) Comparison of the observed drawdowns to the drawdowns modeled by the inverted flow model. (b) Resultant model of the inversion modeling showing the heterogeneous distribution of the transmissivities. (c) Comparison of the result model with the known preferential flow path connectivity (interpreted in the model in dotted blue lines). (d) Superimposition of the known local conduits direction (shown as blue lines) presented in Figure 3c.

shows that it is not directly connected to the main flow network in the model. We noticed that the establishment of this connectivity appeared quickly during the multiscale structural inversion (Figure 4). It indicates the importance of the connectivity between these boreholes toward the reproduction of the global drawdown distribution on the site.

Regarding the knowledge about local conduit direction (Figure 5d), in the inverted model, P8 and P15 are in fact intersecting conduits following the same local direction as observed from downhole videos. In the cases of P5 and P11, where conduits have been observed in the field, the inverted flow network map shows that they intersect preferential flow paths, but not following exactly the same direction as field observations. From the drawdown maps (Figure 6), we can see that simulated pumping in P10 and P17 in our model behave like pumping in the matrix; thus, P10 and P17 are not connected to the karstic network. This is consistent with the information highlighted by camera observations. Only two inverted local flow structures do not reproduce downhole videos observations: P3 seems to be connected to the karstic network; however, no karstic conduits were identified on its downhole video. On the contrary, P9 seems to be located in the matrix in the inverted model, while a conduit has been observed in its borehole video.

In general, the inverted flow network model reconstructs most of the knowledges that we have about the site, even if this information was not used in the inversion process. Thus, it seems that the drawdown data set alone provides sufficient information to reproduce the true network connectivity between boreholes.

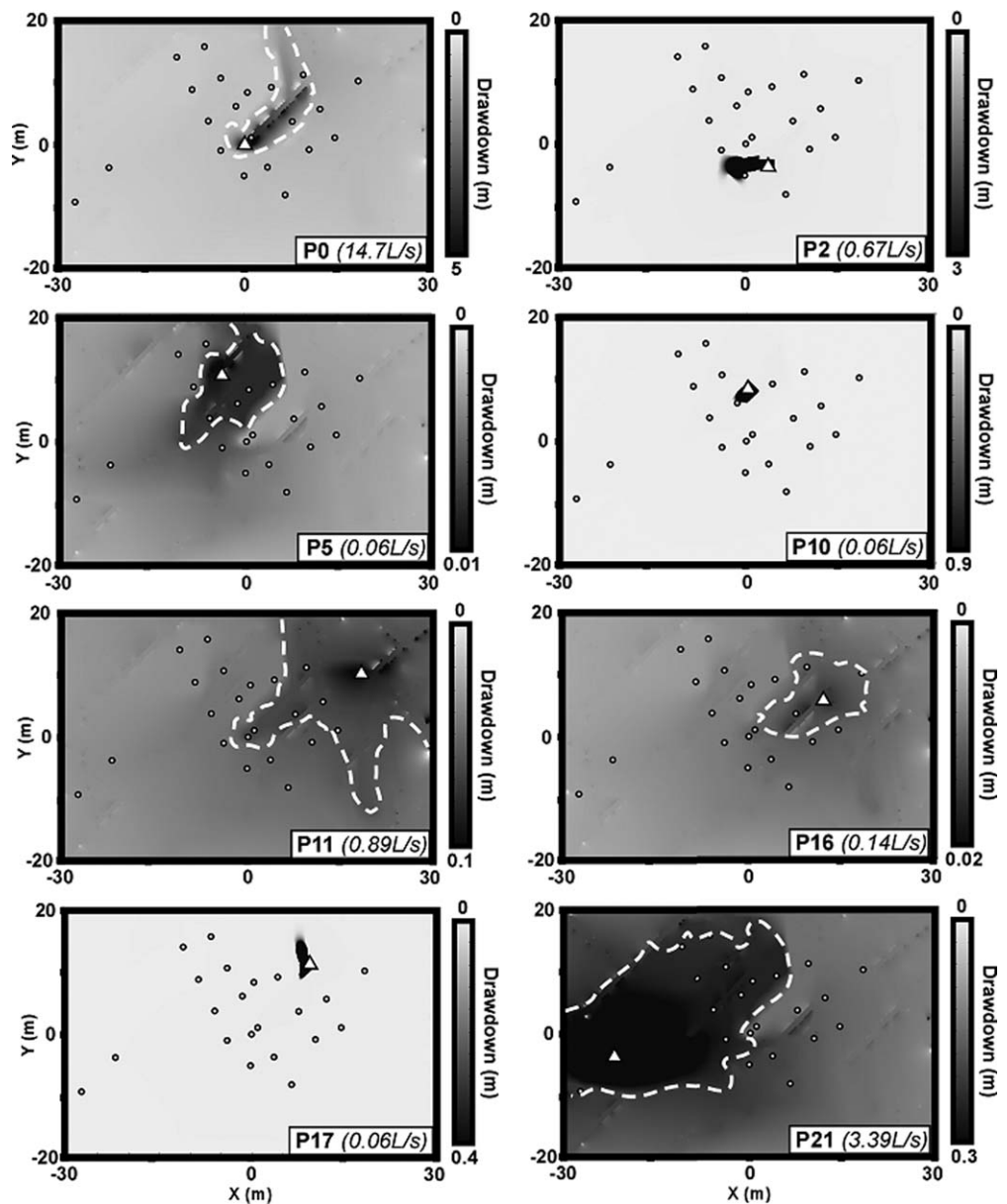


**Figure 6.** Maps of hydraulic drawdowns calculated from the result flow network model. The drawdowns are shown for each of the pumping wells (white triangles) used for the hydraulic tomography (the pumping rate is indicated in each figure). The drawdowns can have very different forms depending on the localization of the borehole in a conduit or in the matrix, highlighting the heterogeneity of the model. Pumping in the matrix (P2, P10, P17) results in a very local drawdown, while pumping in a conduit (P0, P5, P11, P16, P21) produces a more global drawdown in the whole model (in these cases, the area the most impacted by the pumping is delimited by white dotted lines).

Figure 8 presents uncertainty maps, which reflects the reliability of the inversion results, and the areas of the model that are covered by the information given from the different local responses in boreholes. The posterior structural uncertainty map indicates that the structure uncertainty is lower in the center of the model domain than in the periphery. The highest uncertainty in the inverted flow structures (in orange/yellow in Figure 8) occurs consistently in the regions beyond the one constrained by the borehole pattern, where no hydraulic information is available. The most reliable parts of the structure (in blue/green) are located in the middle of the domain, where the borehole pattern is dense, and therefore provides more hydraulic information. The map of the posterior standard deviations of the  $\log_{10}$  transmissivity shows that the matrix transmissivity value is well-constrained only near some boreholes (e.g., P0, P2, P4, P9, P10, P13,

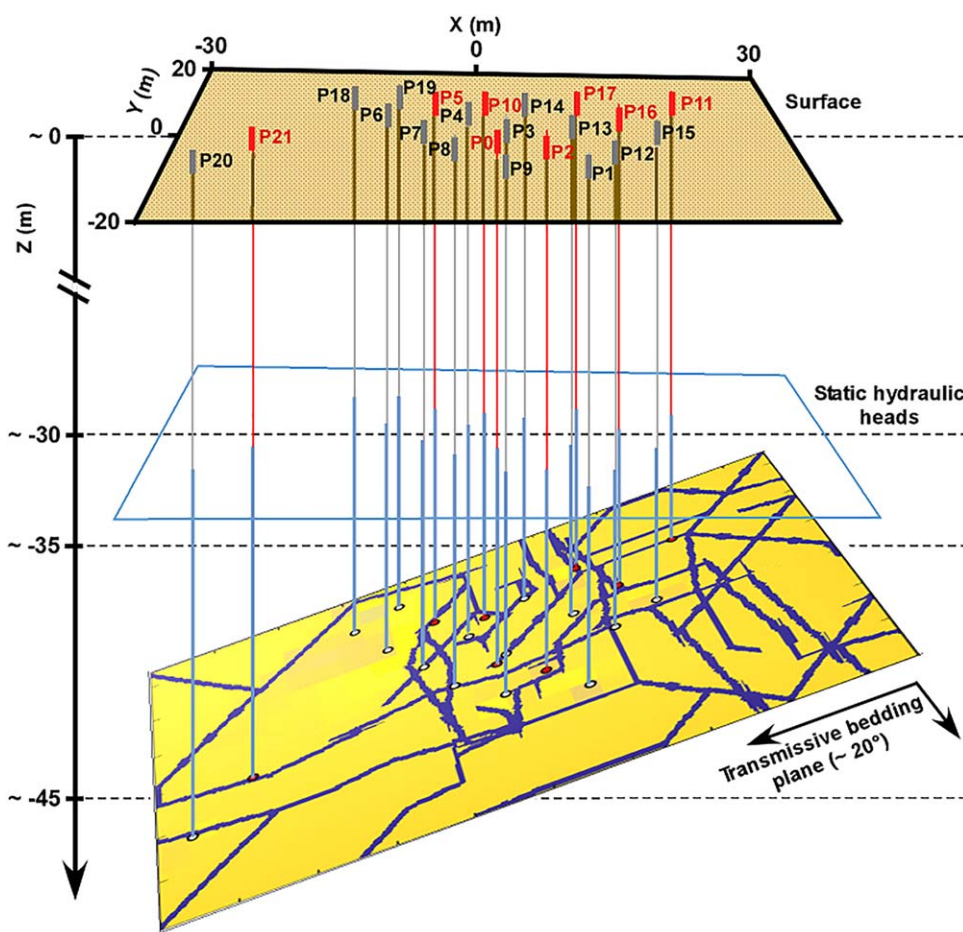


**Figure 7.** Schematic representation of the modeled karstic structure at the Terrieu experimental site, considering the geological information, the hydraulic tomography investigation, and the flow network produced by inversion with the CADI method. The red lines indicate the boreholes where the pumping tests were performed, while the grey lines indicate the measurement boreholes.

and P17). Thus, the pumping tests do not permit a characterization of the bedding plane transmissivity very far from the boreholes.

Figure 9 shows maps of flow velocities for pumping in P0 and P21, the two most productive boreholes, intersected by karstic conduits. The distribution of the modeled flow velocities during each pumping test are controlled by the high-transmissivity karstic features in the model. It appears clearly that the water pumped in these boreholes is mobilized in the karstic network, while the velocity of the water in the bedding plane matrix is low. Even if the CADI method allows a certain imagery of the flow paths that honors the observed hydraulic connectivity to be determined, it may not produce a geomorphologically realistic model. This is caused by the nonunique nature of inverse problem. To provide more realistic karst networks, the hydraulic data should be inverted jointly with other sources of data coming from geophysical and tracer tests or/and constrained by geomorphological and geological information. By comparing the velocity maps for P0 and for P21, we observed that a larger pumping rate (P0) induces an increase of the flow velocities around the borehole, but it also generates a mobilization of water from conduits located further from the pumping borehole, and thus, characterization of a larger area. On the contrary, a lower pumping rate (P21) will more specifically characterize the karstic conduits near the borehole. This implies that the use of transient modeling of a variable pumping rate to characterize both small scale and large scale karstic network would be useful. The velocities maps also indicate that the North-South oriented conduit in the center of the model ( $X = -5$  m) is less solicited by the pumping in P0 and P21. This same conduit is, however, characterized more specifically by a pumping in P5, which would indicate a dual flow direction in the karstic network of the model (N-S and E-W).

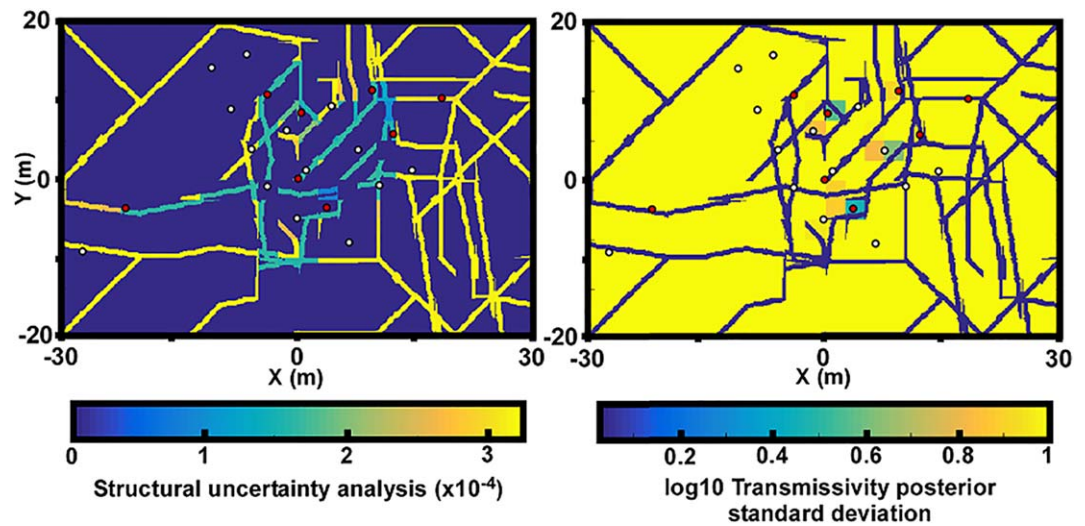


**Figure 8.** The map of the network structural uncertainties (left) shows that the network geometry is well-constrained especially in a zone between each borehole in the center of the model, and compared to the map of transmissivities standard deviation (right), the hydraulic data permitted to constrain more the conduits position than the matrix.

In Figure 10, the inversion result produced by the CADI method is compared to the one produced by the Sparse Nonlinear OPTimizer (SNOPT) method at the same field site and with the same data set (Wang et al., 2016). The SNOPT method is a classical efficient algorithm for nonlinear large-scale inverse problems. The model of Wang et al. (2016) is composed of a grid of squared cells of  $0.5 \times 0.5 \text{ m}^2$ ; each cell is assigned with a transmissivity value, which is optimized in the inversion process. The optimization of the transmissivity values was constrained by upper and lower limits ( $10^{-1}$  and  $10^{-8} \text{ m}^2/\text{s}$ , respectively).

While the CADI method, associated to the multiscale process, can be initialized with a simple model to achieve an inverted flow network consistent with field observations, the SNOPT method required some connectivity information included in the initial model to converge to a coherent model. Overall, the SNOPT and CADI methods generate similar results in terms of medium morphology, where a highly conductive conduit network is embedded in a background matrix. The SNOPT method let more freedom for the optimization of both conduit and matrix transmissivities instead of primarily constraining the flows in a network as done by the CADI method. Thus, it allows establishing a smoother transient of transmissivity from flow paths to the

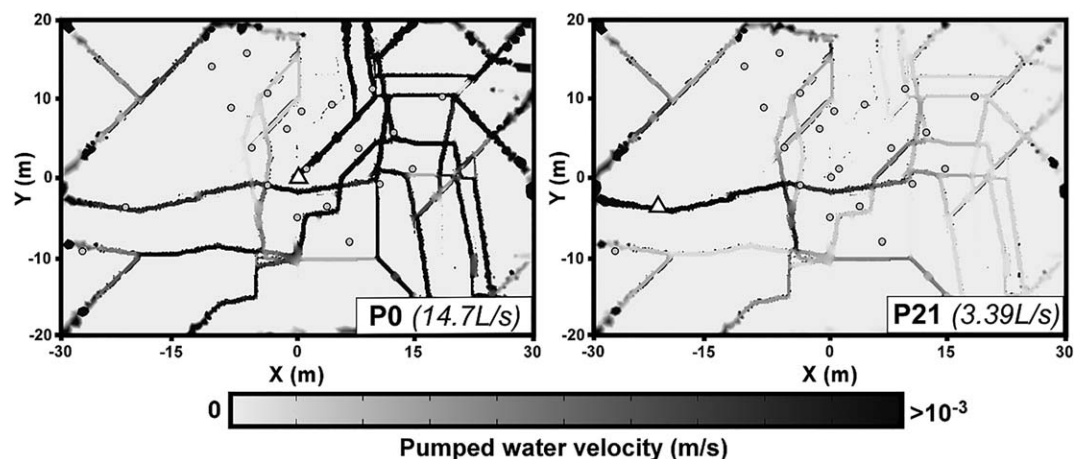


**Figure 9.** Maps of the pumped water velocities calculated by the result model for a pumping in borehole P0 and in borehole P21 (the two most productive pumping). The pumping boreholes are indicated by white triangles. For a reason a better readability of the low velocities, the scale has been fixed on a maximal velocity of  $10^{-3} \text{ m/s}$ , thus in the blackest zones, the velocity can be higher than this value (up to  $10^{-2} \text{ m/s}$  near the pumping point for P0).

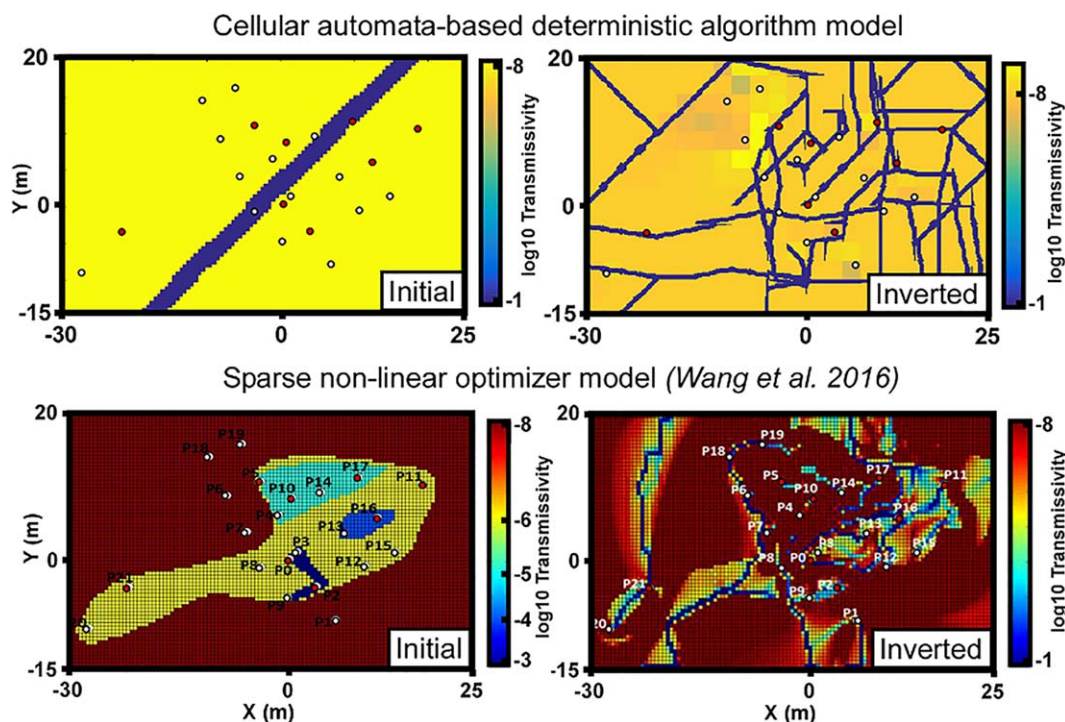


**Figure 10.** Comparison of the inversion result produced by the CADI method and by the SNOPT method (Wang et al., 2016) at the same scale of the Terrieu field site and with same hydraulic data set. The initial models are shown on the left and the inverted models are presented on the right.

background medium. This is important, in some cases, to reproduce the diffusive behavior of local microfissures, which cannot be modeled by the channelized flow in conduits. For this reason, the SNOPT result permits a better reproduction of the measured drawdowns ( $R^2 \sim 0.9$  of SNOPT compared to the  $R^2 \sim 0.78$  of CADI). However, the result by the CADI method is more consistent with the field knowledge of the local conduit orientation and borehole connectivity presented in Figure 3c. The constraints imposed in the CADI method also present the advantage to represent a network in an equivalent porous media result to mimic the hydraulic behaviors in the karstic and fractured environment, thus allowing an easier interpretation of the preferential flow paths positioning and of the connectivity between boreholes.

Although the combination of the CADI method and steady state hydraulic tomography technique appears effective in the identification of flow networks in karstic fields due to its ability of constraining the flows in a network, some limits can be highlighted.

First, we point out that even though the inverted flow paths near the boreholes show a high consistency to field observations, it is possible that some of the inverted conduits may represent the assemble hydraulic behavior of highly fractured areas, while in reality conduits may not be present in those areas. In the same idea, the network in the model is generated with a constant aperture, and thus does not permit to identify the flow paths associated to developed conduits to those associated to fractured zones. To achieve a more realistic network configuration, this method needs to be further developed to include a variable aperture model.

Second, the use of steady state head data may also limit the identification of the preferential paths. In fact, a pumping reaching the steady state in a karstic field mobilizes water in both the conduit network and the fractured rock matrix. The latter tends to blur the hydraulic responses of the conduit network. Using transient data could be useful to improve the inversion result and to reduce the nonuniqueness of the inversion. However, transient inversions may increase significantly the computational demand. A more efficient solution may be to use harmonic pumping (e.g., Rabinovich et al., 2015; Soueid Ahmed et al., 2016). The harmonic data permit to perform inversions in the frequency domain and may highlight the influence of flow from specific components of the system, and therefore would achieve a better characterization of the conduit network.

#### 4. Conclusion

The use of the CADI method for a site scale karstic field characterization shows its capabilities in identifying the preferential flow network. The inverted distributed karstic flow network model reproduces the observed data while maintaining the realism of a highly heterogeneous flows distribution. The constraints imposed for the inversion process result in a model that localizes the conduits of the karstic network, which in turn control the main drawdowns direction.

The use of hydraulic tomography data in the inversion permits the characterization of the highly heterogeneous discrete conduit network. However, this requires a large number of boreholes, and, especially boreholes intersecting the karstic network. Results of the flow velocities in P0 and P21 show that pumping in boreholes intersecting the karstic network with different pumping rate could characterize the network at different scales (locally or more globally). This promotes the use, in the future, of the recently developed harmonic pumping technique at the Terrieu experimental site to identify more precisely the geometry of the karstic network with less pumping tests.

Some necessary conditions were met in the case of the Terrieu experimental site to successfully apply the CADI method. The karstic network at this site was mainly constrained within a bedding plane, which permits a two-dimensional modeling. Also, the subsurface flow in the Terrieu site is constrained mainly by the karstic conduits, while the matrix has a very low transmissivity. This permitted the model to start from an assumption of a two domain site (matrix and conduit), distinguished by a high contrast in transmissivity. In the future, the current method will be further developed to deal with transient hydraulic data and/or to use harmonic pumping responses, which are more sensitive to the karst connectivity, for improving the characterization of the geometry of the conduit networks.

#### Acknowledgments

We thank the Normandy region for providing financial support for the PhD of Pierre Fischer. We would like to thank three anonymous reviewers for their relevant comments and corrections which permitted to significantly improve the quality of this article. The hydraulic data collection and hydrogeological characterization of the Terrieu experimental site presented in this work are the property of the French research network SO Karst and are freely accessible on demand to a person in charge of the network (see [www.sokarst.org](http://www.sokarst.org) for more information about the SO Karst institution and contacts).

#### References

- Abusaada, M., & Sauter, M. (2013). Studying the flow dynamics of a karst aquifer system with an equivalent porous medium model. *Ground Water*, 51(4), 641–650.
- Arfib, B., & Charlier, J.-B. (2016). Insights into saline intrusion and freshwater resources in coastal karstic aquifers using a lumped Rainfall-Discharge-Salinity model (the Port-Miou brackish spring, SE France). *Journal of Hydrology*, 540, 148–161.
- Bohling, G. C., Zhan, X., Butler, J. J. Jr., & Zheng, L. (2002). Steady shape analysis of tomographic pumping tests for characterization of aquifer heterogeneities. *Water Resources Research*, 38(12), 1324. <https://doi.org/10.1029/2001WR001176>
- Cardiff, M., Barrash, W., Kitanidis, P. K., Malama, B., Revil, A., Straface, S., & Rizzo, E. (2009). A potential-based inversion of unconfined steady-state hydraulic tomography. *Ground Water*, 47(2), 259–270.
- Cardiff, M., & Kitanidis, P. K. (2009). Bayesian inversion for facies detection: An extensible level set framework. *Water Resources Research*, 45: W10416. <https://doi.org/10.1029/2008WR007675>
- Castagna, M., Becker, M. W., & Bellin, A. (2011). Joint estimation of transmissivity and storativity in a bedrock fracture. *Water Resources Research*, 47, W09504. <https://doi.org/10.1029/2010WR009262>
- Dausse, A. (2015). *Facteurs d'échelle dans la hiérarchisation des écoulements au sein d'un aquifère karstique: Analyse multi-échelles des propriétés hydrodynamiques et de transport de l'aquifère de Lez* (PhD thesis), French: Université de Montpellier.
- Dreiss, S. J. (1982). Linear kernels for Karst aquifers. *Water Resources Research*, 18, 865–876.
- Fischer, P., Jardani, A., & Lecoq, N. (2017b). A cellular automata-based deterministic inversion algorithm for the characterization of linear structural heterogeneities. *Water Resources Research*, 53, 2016–2034. <https://doi.org/10.1002/2016WR019572>
- Fischer, P., Jardani, A., Soueid Ahmed, A., Abbas, M., Wang, X., Jourde, H., & Lecoq, N. (2017a). Application of large-scale inversion algorithms to hydraulic tomography in an alluvial aquifer. *Ground Water*, 55, 208–218.
- Ghasemzadeh, R., Hellweger, F., Butscher, C., Padilla, I., Vesper, D., Field, M., & Alshwabkeh, A. (2012). Review: Groundwater flow and transport modeling of karst aquifers, with particular reference to the North Coast Limestone aquifer system of Puerto Rico. *Hydrogeology Journal*, 20, 1441–1464.
- Grimstadt, A.-A., Mannseth, T., Naevdal, G., & Urkedal, H. (2003). Adaptive multiscale permeability estimation. *Computers & Geosciences*, 7(1), 1–25.
- Hartmann, A., Goldscheider, N., Wagener, T., Lange, J., & Weiler, M. (2014a). Karst water resources in a changing world: Review of hydrological modeling approaches. *Reviews of Geophysics*, 52, 218–242.
- Hartmann, A., Mudarra, M., Andreo, B., Marin, A., Wagener, T., & Lange, J. (2014b). Modeling spatiotemporal impacts of hydroclimatic extremes on groundwater recharge at a Mediterranean karst aquifer. *Water Resources Research*, 50, 6507–6521. <https://doi.org/10.1002/2014WR015685>
- Hoeksema, R. J., & Kitanidis, P. K. (1984). An application of the geostatistical approach to the inverse problem in two-dimensional groundwater modeling. *Water Resources Research*, 20, 1003–1020.
- Jaquet, O., Siegel, P., Klubertanz, G., & Benabderrhamane, H. (2004). Stochastic discrete model of karstic networks. *Advances in Water Resources*, 27, 751–760.
- Jazayeri Noushabadi, M. R. (2009). *Characterization of relationship between fracture network and flow-path network in fractured and karstic reservoirs: Numerical modeling and field investigation (Lez aquifer, Southern France)* (PhD thesis). France: Université de Montpellier.
- Jazayeri Noushabadi, M. R., Jourde, H., & Massonnat, G. (2011). Influence of the observation scale on permeability estimation at local and regional scales through well tests in a fractured and karstic aquifer (Lez aquifer, Southern France). *Journal of Hydrology*, 403, 321–336.

- Jourde, H., Batiot-Guilhe, C., Bailly-Comte, V., Bicalho, C., Blanc, M., Borrell, V., . . . Van-Exter, S. (2011). The MEDYCYSS observatory, a multi scale observatory of flood dynamics and hydrodynamics in karst (Mediterranean border Southern France). In N. Lambrakis, G. Stournaras, & K. Katsanou (Eds.), *Advances in the research of aquatic environment*. Environmental earth sciences. Berlin, Heidelberg: Springer.
- Jourde, H., Cornaton, F., Pistre, S., & Bidaux, P. (2002). Flow behavior in a dual fracture network. *Journal of Hydrology*, 266, 99–119.
- Kong-A-Siou, L., Johannet, A., Borrell Estupina, V., & Pistre, S. (2015). Neural networks for karst groundwater management: Case of the Lez spring (Southern France). *Environmental Earth Sciences*, 74, 7617–7632.
- Kordilla, J., Sauter, M., Reimann, T., & Geyer, T. (2012). Simulation of saturated and unsaturated flow in karst systems at catchment scale using a double continuum approach. *Hydrology of Earth System Sciences*, 16, 3909–3923.
- Kovacs, A., & Sauter, M. (2007). Modelling karst hydrodynamics. In N. Goldscheider & D. Drew (Eds.), *Methods in karst hydrogeology* (pp. 65–91). London, UK: Taylor & Francis/Balkema.
- Labat, D., Ababou, R., & Mangin, A. (1999). Linear and nonlinear input/output models for karstic springflow and flood prediction at different time scales. *Stochastic Environmental Research and Risk Assessment*, 13, 337–364.
- Ladouche, B., Marechal, J.-C., & Dorfliger, N. (2014). Semi-distributed lumped model of a karst system under active management. *Journal of Hydrology*, 509, 215–230.
- Lee, J., & Kitanidis, P. K. (2013). Bayesian inversion with total variation prior for discrete geologic structure identification. *Water Resources Research*, 49, 7658–7669. <https://doi.org/10.1002/2012WR013431>
- Lee, J., & Kitanidis, P. K. (2014). Large-scale hydraulic tomography and joint inversion of head and tracer data using the principal component geostatistical approach (PCGA). *Water Resources Research*, 50, 5410–5427. <https://doi.org/10.1002/2014WR015483>
- Long, A. J., & Derickson, R. G. (1999). Linear systems analysis in a karst aquifer. *Journal of Hydrology*, 219, 206–217.
- Pianosi, F., Beven, K., Freer, J., Hall, J. W., Rougier, J., Stephenson, D. B., & Wagener, T. (2016). Sensitivity analysis of environmental models: A systematic review with practical workflow. *Environmental Modelling & Software*, 79, 214–232.
- Rabinovich, A., Barrash, W., Cardiff, M., Hochstetler, D. L., Bakhos, T., Dagan, G., & Kitanidis, P. K. (2015). Frequency dependent hydraulic properties estimated from oscillatory pumping tests in an unconfined aquifer. *Journal of Hydrology*, 531, 2–16.
- Saller, S. P., Ronayne, M. J., & Long, A. J. (2013). Comparison of a karst groundwater model with and without discrete conduit flow. *Hydrogeology Journal*, 21, 1555–1566.
- Sharmeen, R., Illman, W. A., Berg, S. J., Yeh, T.-C. J., Park, Y.-J., Sudicky, E. A., & Ando K. (2012). Transient hydraulic tomography in a fractured dolostone: Laboratory rock block experiments. *Water Resources Research*, 48. <https://doi.org/10.1029/2012WR012216>
- Soueid Ahmed, A., Jardani, A., Revil, A., & Dupont, J. P. (2016). Joint inversion of hydraulic head and self-potential data associated with harmonic pumping tests. *Water Resources Research*, 52, 6769–6791. <https://doi.org/10.1002/2016WR019058>
- Tarantola, A., & Valette, B. (1982). Generalized nonlinear inverse problems solved using the least squares criterion. *Reviews of Geophysics and Space Physics*, 20(2), 219–232.
- Von Neumann, J., & Burks, A. W. (1966). *Theory of self-reproducing automata*. Champaign, IL: University of Illinois Press.
- Wang, X., Jardani, A., & Jourde, H. (2017). A hybrid inverse method for hydraulic tomography in fractured and karstic media. *Journal of Hydrology*, 551, 29–46.
- Wang, X., Jardani, A., Jourde, H., Lonergan, L., Cosgrove, J., Gosselin, O., & Massonat, G. (2016). Characterisation of the transmissivity field of a fractured and karstic aquifer, Southern France. *Advances in Water Resources*, 87, 106–121.
- White, W. B. (2002). Karst hydrology: Recent developments and open questions. *Engineering Geology*, 65, 85–105.
- Yeh, T.-C. J., & Liu, S. (2000). Hydraulic tomography: Development of a new aquifer test method. *Water Resources Research*, 36, 2095–2105.
- Zhu, J., & Yeh, T.-C. J. (2005). Characterization of aquifer heterogeneity using transient hydraulic tomography. *Water Resources Research*, 41, W07028. <https://doi.org/10.1029/2004WR003790>
- Zimmerman, R. W., Chen, G., Hadgu, T., & Bodvarsson, G. S. (1993). A numerical dual-porosity model with semianalytical treatment of fracture/matrix flow. *Water Resources Research*, 29, 2127–2137.